

# Observation of stacking engineered magnetic phase transitions within moiré supercells of twisted van der Waals magnets

Senlei Li<sup>1,+</sup>, Zeliang Sun<sup>2,+</sup>, Nathan J. McLaughlin<sup>3</sup>, Afsana Sharmin<sup>4</sup>, Nishkarsh Agarwal<sup>5</sup>, Mengqi Huang<sup>1</sup>, Suk Hyun Sung<sup>5</sup>, Hanyi Lu<sup>3</sup>, Shaohua Yan<sup>6,7</sup>, Hechang Lei<sup>6,7</sup>, Robert Hovden<sup>5</sup>, Hailong Wang<sup>1</sup>, Hua Chen<sup>4,8</sup>, Liuyan Zhao<sup>2,\*</sup>, and Chunhui Rita Du<sup>1,3,\*</sup>

<sup>1</sup>School of Physics, Georgia Institute of Technology, Atlanta, Georgia 30332, USA

<sup>2</sup>Department of Physics, the University of Michigan, Ann Arbor, Michigan 48109, USA

<sup>3</sup>Department of Physics, University of California, San Diego, La Jolla, California 92093, USA

<sup>4</sup>Department of Physics, Colorado State University, Fort Collins, Colorado 80523, USA

<sup>5</sup>Department of Materials Science and Engineering, University of Michigan, Ann Arbor, Michigan 48109, USA

<sup>6</sup>Beijing Key Laboratory of Optoelectronic Functional Materials MicroNano Devices, Department of Physics, Renmin University of China, Beijing 100872, China

<sup>7</sup>Key Laboratory of Quantum State Construction and Manipulation (Ministry of Education), Renmin University of China, Beijing, 100872, China

<sup>8</sup>School of Advanced Materials Discovery, Colorado State University, Fort Collins, Colorado 80523, USA

\*Corresponding authors: [lyzhao@umich.edu](mailto:lyzhao@umich.edu); [cdu71@gatech.edu](mailto:cdu71@gatech.edu)

<sup>+</sup>These authors contributed equally.

**Abstract:** Twist engineering of magnetic van der Waals (vdW) moiré superlattices provides an attractive way to achieve precise nanoscale control over the spin degree of freedom on two-dimensional flatland. Despite the very recent demonstrations of moiré magnetism featuring exotic phases with noncollinear spin order in twisted vdW magnet chromium triiodide CrI<sub>3</sub>, the local magnetic interactions, spin dynamics, and magnetic phase transitions within and across individual moiré supercells remain elusive. Taking advantage of a scanning single-spin magnetometry platform, here we report observation of two distinct magnetic phase transitions with separate critical temperatures within a moiré supercell of small-angle twisted double trilayer CrI<sub>3</sub>. By measuring temperature dependent spin fluctuations at the coexisting ferromagnetic and antiferromagnetic regions in twisted CrI<sub>3</sub>, we explicitly show that the Curie temperature of the ferromagnetic state is higher than the Néel temperature of the antiferromagnetic one by ~10 K. Our mean-field calculations attribute such a spatial and thermodynamic phase separation to the stacking order modulated interlayer exchange coupling at the twisted interface of the moiré superlattices. The presented results highlight twist engineering as a promising tuning knob to realize on-demand control of not only the nanoscale spin order of moiré quantum matter but also its dynamic magnetic responses, which may find relevant applications in developing transformative vdW electronic and magnetic devices.

Recently, twisted two-dimensional (2D) van der Waals (vdW) magnets have emerged as a new member in the suite of moiré quantum materials, where the spin degree of freedom is controlled through the local stacking order of moiré superlattices<sup>1–11</sup>. As opposed to moiré quantum electronic matter such as twisted graphene<sup>12–15</sup> and transition metal dichalcogenides<sup>14–16</sup> that feature enhanced electronic interactions from moiré flat-bands, moiré magnets rely on twist engineered magnetic interaction competitions to realize unconventional magnetic orders and spin excitations over moiré wavelengths, for example, in twisted vdW magnet chromium triiodide CrI<sub>3</sub><sup>1–5,7–9,11</sup>.

Few-layer CrI<sub>3</sub> shows stacking dependent interlayer magnetic exchange coupling that is ferromagnetic (FM) for the rhombohedral stacking and antiferromagnetic (AFM) for the monoclinic stacking geometry<sup>8,17–19</sup>, whereas the intralayer exchange coupling is FM with a strong out-of-plane easy-axis anisotropy<sup>8,17,18</sup>. In twisted CrI<sub>3</sub> with spatially distributed rhombohedral and monoclinic stacking geometries, the competition between uniform FM intralayer exchange coupling and FM-AFM modulated moiré interlayer exchange interaction drives the formation of a range of novel magnetic orders, such as coexisting FM and AFM states within moiré supercells in twisted bilayer and double trilayer CrI<sub>3</sub><sup>1,2</sup>, and emergent magnetization and noncollinear spins in twisted double bilayer CrI<sub>3</sub><sup>3–5</sup>. So far, the ongoing research on twisted CrI<sub>3</sub> has mainly focused on investigating spatially modulated magnetic orders of the ground states<sup>1–5,11</sup>, which represents only a subset of information about moiré magnetism. The local magnetic interactions, spin dynamics, and magnetic phase transitions within and across moiré supercells awaits exploration and is necessary for developing a comprehensive picture of moiré magnetism.

Here, we report scanning single-spin quantum sensing<sup>20–22</sup> of both static magnetization and dynamic spin fluctuations of moiré magnetism hosted by twisted double trilayer (tDT) CrI<sub>3</sub> across the second-order magnetic phase transition points ( $T_c$ ). We show that the FM region within individual moiré supercells formed in small-twist-angle tDT CrI<sub>3</sub> exhibit a higher  $T_c$  up to  $\sim 58$  K in comparison with that of  $\sim 48$  K for their AFM counterparts resulting in a nanoscale co-existing paramagnetic(PM)-ferromagnetic(FM) phase in an intermediate temperature regime ( $48 \text{ K} < T < 58 \text{ K}$ ), while such a phenomenon is absent in the large-twist-angle regime. Our experimental results are well explained by a proposed mean-field theoretical model of layer-resolved magnetic phases of tDT CrI<sub>3</sub> taking account of stacking engineered exchange interactions at the twisted interface. The current work highlights twist engineering as a promising tuning knob to realize local control of magnetic responses at individual stacking sites, which could contribute to a broad range of emerging 2D electronic applications<sup>23,24</sup>. The new insights on moiré magnetism presented in this study further highlight the potential of quantum metrology tools<sup>20</sup> in exploring unconventional spin related phenomena in correlated magnetic quantum states of matter.

We first briefly review the pertinent material properties of tDT CrI<sub>3</sub>, which provides a reliably high-quality moiré magnet platform for the current study<sup>2</sup>. Figure 1a shows a moiré superlattice structure formed by stacking two CrI<sub>3</sub> trilayers with a small twist angle. The local atomic registry exhibits a periodic modulation in real space, leading to spatially alternating stacking geometries on a length scale of moiré wavelengths<sup>1–3</sup>. At the monoclinic (AB') stacking site, the two CrI<sub>3</sub> trilayers are coupled by a positive exchange interaction  $J_M$ , leading to local AFM order at the twisted interface with a fully compensated net magnetic moment in the ground state<sup>2,8</sup>. In contrast, FM order with a net magnetic moment is established at the rhombohedral (AB) stacking site driven by a negative interlayer exchange interaction  $J_R$ <sup>2,8</sup>. Using first-principles calculations, theoretical study has reported that the magnitude of  $J_R$  could be one order of magnitude larger than that of  $J_M$  due to the orbital dependent exchange coupling<sup>8</sup>. Fundamentally,

the sign and magnitude of magnetic interactions in twisted CrI<sub>3</sub> not only determine its local magnetic phases but also affect their dynamic responses to external perturbations. The former has been predicted and experimentally demonstrated recently<sup>2,8</sup>, and the latter is the focus of the current work.

We fabricated tDT CrI<sub>3</sub> devices by the standard “tear-and-stack” technique and encapsulated them with hexagonal boron nitride (hBN) nanoflakes<sup>1-3,12,25</sup>. The samples for transmission electron microscopy and quantum sensing measurements were fabricated separately because they required different substrates for individual measurement purposes (See Methods Section for details). Selected area electron diffraction (SAED) patterns (Fig. 1b) of a surveyed sample area of a tDT CrI<sub>3</sub> device shows sets of the fifth-order Bragg peaks with sixfold rotation symmetry. The local mean twist angle is measured to be  $0.8^\circ \pm 0.1^\circ$  by fitting 2D gaussians to the diffraction peaks, giving a moiré period of  $\sim 50$  nm. Such an intermediate twist angle ensures a decent, regular moiré lattice structure formed in tDT CrI<sub>3</sub> that is visible in transmission electron microscopy measurements. Figure 1c presents a bright-field transmission electron microscopy (BF-TEM) image with contrast similar to the fifth-order Bragg peaks, which shows the characteristic hexagonal superlattice structures with a periodicity commensurate with the moiré wavelength. The distortions from the expected moiré lattice patterns could be induced by lattice strain, relaxation, and local structural inhomogeneities (see Supplementary Information Note 1 for details)<sup>26</sup>.

Next, we utilize scanning nitrogen-vacancy (NV) microscopy<sup>2,18,27-29</sup> to spatially resolve the moiré magnetism hosted by tDT CrI<sub>3</sub> as illustrated in Fig. 2a. Scanning NV magnetometry exploits the Zeeman effect to quantitatively detect local magnetic stray fields longitudinal to the NV spin axis<sup>21</sup>. The magnitude of the magnetic field is directly related to the splitting of NV spin energies, which can be read out by optically detected magnetic resonance measurements<sup>2,18</sup> (see Supplementary Information Note 2 for details). The spatial resolution of scanning NV magnetometry is primarily determined by the NV-to-sample distance<sup>30</sup>, which is  $\sim 70$  nm in our measurements (see Supplementary Information Note 3 for details). In the current study, we report scanning NV quantum sensing measurements of a total of three twisted vdW magnet samples:  $0.15^\circ$  tDT CrI<sub>3</sub>,  $0.25^\circ$  tDT CrI<sub>3</sub>, and  $15^\circ$  tDT CrI<sub>3</sub>. For the brevity of our narrative,  $0.15^\circ$  and  $0.25^\circ$  refer to the small twist angle, and  $15^\circ$  refers to the large twist angle in our description.

Figure 2b shows a microscope image of a prepared tDT CrI<sub>3</sub> sample with a calibrated local twist angle  $\alpha = 0.15^\circ$  and an expected moiré period of  $\sim 250$  nm. Note that in order to visualize nanoscale magnetic patterns within individual moiré supercells, here  $\alpha$  is chosen to be smaller than  $\sim 0.5^\circ$ , ensuring that the resulting moiré period is larger than our NV spatial sensitivity ( $\sim 70$  nm). Figure 2c presents a stray field  $B_F$  map measured on a selected sample area of the  $0.15^\circ$  tDT CrI<sub>3</sub> device at 2 K. An external magnetic field of  $\sim 2,000$  G is applied along the NV spin axis in this measurement. The tDT CrI<sub>3</sub> sample shows clear multidomain features with stray fields of opposite polarity emanating from individual domains. The reconstructed out-of-plane magnetization ( $m_z$ )<sup>2,18</sup> map (Fig. 2d) manifests alternating FM and AFM patches on a length scale comparable with the moiré period (see Supplementary Information Note 4 for details). The local net magnetization is measured to be 0 and  $\sim 30 \mu_B/\text{nm}^2$  for the AFM and FM domains, respectively, exhibiting the key feature of stacking induced co-existing magnetic phases of moiré magnetism<sup>1,2</sup> (see Supplementary Information Note 5 for details). The measured local magnetization of FM order in  $0.15^\circ$  tDT CrI<sub>3</sub> also agrees with the theoretical value  $29.4 \mu_B/\text{nm}^2$ <sup>18</sup>. By performing an autocorrelation operation<sup>2</sup> on the magnetization map, the periodic hexagonal shaped magnetic patterns of tDT CrI<sub>3</sub> is revealed in Fig. 2e, from which the local mean twist angle ( $\alpha = 0.15^\circ$ ) and moiré period ( $\sim 250$  nm) are

confirmed. The notable alternating FM-AFM state is also observed in another  $0.25^\circ$  tDT CrI<sub>3</sub> device (Figs. 2f-2h). It is worth mentioning that a larger twist angle naturally results in spatially more compact magnetic moiré patterns (Fig. 2g) with a reduced moiré period of  $\sim 150$  nm (Fig. 2h).

We now present systematic scanning NV magnetometry measurements to show distinct magnetic phase transition temperatures for the observed FM and AFM states within individual moiré supercells. Figure 3a presents a zoomed-in magnetization map of a selected sample area of the  $0.15^\circ$  tDT CrI<sub>3</sub> device, showing two neighboring nanoscale FM and AFM domains. Due to the fully compensated net magnetic moment, temperature driven second-order magnetic phase transition of the AFM domain in tDT CrI<sub>3</sub> is challenging to access by measuring its emanating magnetic flux. To circumvent this issue, here we employ NV relaxometry method<sup>27,31-35</sup> to probe the intrinsic spin fluctuations at the local AFM (FM) regions. Figure 3b illustrates the mechanism of scanning NV relaxometry measurements, which takes advantage of the dipole-dipole interaction between local spin fluctuations of AFM (FM) spin density and a proximal NV center contained in a diamond cantilever. Spin fluctuations in a magnetically correlated system are driven by its time dependent spin density distribution, for example, due to the dynamic imbalance in the thermal occupation of magnon bands with opposite chiralities<sup>31,34,36</sup>. For both AFM and FM systems with (un)compensated net static magnetic moment, spin-spin correlation induced time dependent fluctuations of the average spin density do not vanish and are expected to reach a maximum intensity around the magnetic phase transition points<sup>33,34</sup>. The emanating fluctuating magnetic fields at the NV electron spin resonance (ESR) frequencies will induce NV spin transitions from the  $m_s = 0$  to  $m_s = \pm 1$  state, resulting in enhancement of the corresponding NV spin relaxation rates<sup>27,32,33,36</sup>. By measuring the spin-dependent NV photoluminescence, the occupation probabilities of NV spin states can be quantitatively obtained, allowing for extraction of NV spin relaxation rate that is proportional to the magnitude of the local fluctuating magnetic fields transverse to the NV axis (see Supplementary Information Note 6 for details)<sup>27,32-34</sup>. Figure 3c shows the measured temperature dependent NV spin relaxation rate  $\Gamma$  when the NV center is positioned right above the FM (AFM) domain formed in the  $0.15^\circ$  tDT CrI<sub>3</sub> sample (Fig. 3a). Due to the divergent magnetic susceptibility, the measured NV spin relaxation rate shows a clear enhancement across the second-order magnetic phase transition points of tDT CrI<sub>3</sub>, from which the Curie and Néel temperatures of the co-existing FM-AFM states are measured to be  $\sim 58$  K and  $\sim 48$  K, respectively. We would like to highlight that similar experimental signatures are also observed in the  $0.25^\circ$  tDT CrI<sub>3</sub> sample as detailed in Supplementary Information Note 7. It is worth noting that twist induced lattice reconstructions for small twist angles typically happen at the boundary of different stacking areas within individual moiré supercells in tDT CrI<sub>3</sub><sup>37</sup>, so the potential strain effect would play a marginal role in our measurements here.

At the monoclinic (AB') stacking sites, tDT CrI<sub>3</sub> features the same type AFM interlayer interaction across the six CrI<sub>3</sub> layers, thus it is not surprising that the formed local AFM moment manifests a similar  $T_c$  with that of the atomically thin pristine CrI<sub>3</sub> crystals studied in previous work (see Supplementary Information Note 8 for details)<sup>8,17,38</sup>. In contrast, the FM order established in tDT CrI<sub>3</sub> is driven by rhombohedral (AB) stacking featuring an enhanced, negative interlayer exchange coupling at the twisted interface<sup>8,39</sup>. Intuitively, such a stronger magnetic interaction will render the magnetic ordering more robust against thermal perturbations, resulting in an increased  $T_c$  of the local FM state formed in tDT CrI<sub>3</sub>. It is instructive to note that the  $T_c$  (or  $T_c$ -equivalent) defined in the current manuscript for the FM order in tDT CrI<sub>3</sub>, an “inhomogeneous” magnetic system along the thickness direction, has considered the overall magnetic contributions

from all the six CrI<sub>3</sub> monolayers. Our one-dimensional (1D) scanning NV relaxometry measurements across the FM-AFM domains (Fig. 3d) further confirm this point. When  $T = 48$  K, one can see that the measured 1D NV spin relaxation spectrum shows a peak value at the corresponding AFM domain site. As the temperature increases to 58 K, the observed peak of NV relaxation rate shifts to the FM domain side, demonstrating that the coexisting FM-AFM states show distinct magnetic phase transition temperatures. Note that such an experimental feature is absent in NV relaxation measurements performed at 38 K and 65 K, when the temperature is away from the Curie (Néel) points of FM (AFM) domains in 0.15° tDT CrI<sub>3</sub>.

After showing the nanoscale stacking engineered  $T_c$  of moiré magnetism, next, we present temperature dependent magnetization maps to provide an alternative perspective to examine the second-order magnetic phase transitions in tDT CrI<sub>3</sub>. Figures 4a and 4b present reconstructed out-of-plane magnetization ( $m_z$ ) maps of the 0.15° and 0.25° tDT CrI<sub>3</sub> devices measured at 38 K. It is evident that rhombohedral (AB) stacking induced FM state in tDT CrI<sub>3</sub> features uncompensated net magnetization. As the temperature increases, the FM moment in tDT CrI<sub>3</sub> gradually decreases and remains robust at 46 K (Figs. 4d and 4e). Figure 4g plots temperature dependence of the average out-of-plane magnetization  $\bar{m}_z$  of FM domains formed in the selected sample areas of 0.15° and 0.25° tDT CrI<sub>3</sub> devices, from which the corresponding Curie point is obtained to be ~58 K, in agreement with our NV relaxometry results. Note that in the small twist angle regime, local moiré lattices relax to the monoclinic (AB') and rhombohedral (AB) stacking sites whose magnetic ground states follow their naturally preferred state. Under this condition, the interlayer exchange energy in tDT CrI<sub>3</sub> is dominated by the local stacking order, and the (small) twist angle plays a secondary role. Thus, the interlayer exchange energy of 0.15° and 0.25° tDT CrI<sub>3</sub> are basically the same, leading to the (almost) identical temperature dependent magnetic phase transition behaviors. To further investigate stacking order dependent magnetic response in tDT CrI<sub>3</sub>, Fig. 4c presents a magnetization map of a 15° tDT CrI<sub>3</sub> device measured at 38 K. Notably, the co-existing FM-AFM phase disappears while a pure collinear FM ground state emerges in the large-twist-angle regime<sup>1</sup>. It is worth mentioning that the two CrI<sub>3</sub> trilayers are weakly ferromagnetically coupled at the twisted interface of 15° tDT CrI<sub>3</sub>, resulting in a reduced Curie temperature (~48 K) in comparison with that of the small-twist-angle tDT CrI<sub>3</sub>. One can see that the 15° tDT CrI<sub>3</sub> sample enters the paramagnetic phase showing zero net FM moment at 48 K (Fig. 4f). To better illustrate this point, Fig. 4h presents the histograms of Curie temperatures of individual FM domains formed in 0.15°, 0.25°, and 15° tDT CrI<sub>3</sub> devices. Statistically, it is evident that FM domains in small-twist-angle tDT CrI<sub>3</sub> show clearly higher Curie temperatures than their counterparts in large-twist-angle tDT CrI<sub>3</sub> (see Supplementary Information Note 9 for details).

We now present a mean-field theoretical model of atomically layer-resolved magnetic order to explain the nanoscale stacking dependent magnetic phase transitions observed in small-twist-angle tDT CrI<sub>3</sub>. Our model consists of layer-uniform Ising spins representing out-of-plane magnetic moments of Cr atoms in tDT CrI<sub>3</sub> as shown in Fig. 5a. The intra-layer magnetic exchange interaction  $J_i$ , stacking-dependent monoclinic (AB') type interlayer exchange interaction  $J_M$ , and rhombohedral (AB) type interlayer exchange interaction  $J_R$  in tDT CrI<sub>3</sub> are obtained to be -1.32 meV, 0.086 meV, and -0.99 meV by comparing mean-field theory results with existing experimental transition temperatures and/or theoretically predicted values (See Method Section and Supplementary Information Note 10 for details)<sup>40</sup>. We compare the mean-field phases of tDT CrI<sub>3</sub> with a uniform monoclinic stacking (bottom panel of Fig. 5a) and rhombohedral stacking at the twisted interface (top panel of Fig. 5a), approximating the situation for regions deep inside different stacking domains. The case of monoclinic stacking features the same exchange coupling

between all neighboring layers and should therefore show a single Néel transition at the temperature scale set by  $J_i$  and  $J_M$ . However, for the rhombohedral stacking case, the much stronger  $J_R$  (in comparison with  $J_M$ ) between the two middle CrI<sub>3</sub> layers (layer 3 and layer 4 shown in Fig. 5a) is expected to drive the system through an FM transition at a higher temperature. To corroborate the above physical picture, we have solved the mean-field equations of our model to get the temperature dependence of the normalized out-of-plane magnetization of individual CrI<sub>3</sub> layers as shown in Figs. 5b and 5c (See Supplementary Information Note 10 for details). In the rhombohedral (AB) stacking region (Fig. 5b), one can see that the middle CrI<sub>3</sub> layer (layer 3) indeed exhibits a higher  $T_c \sim 58$  K in comparison with that of  $\sim 48$  K for the monoclinic (AB') stacking case (Fig. 5c). Moreover, in the AB stacking case the mean-field magnetic moments of the two top CrI<sub>3</sub> monolayers (layer 1 and layer 2) undergo a smooth crossover as temperature decreases below  $T_c$  before reaching the saturated value but not another phase transition as dictated by the Lee-Yang theorem<sup>41</sup>. By considering the overall contributions from all the six CrI<sub>3</sub> layers, the effective Curie temperature ( $T_c$ -equivalent) of stacking induced FM order in small-twist-angle tDT CrI<sub>3</sub> is calculated to be 58 K, in agreement with our NV measurement results. In contrast, in the monoclinic (AB') stacking case (Fig. 5c), the top and middle CrI<sub>3</sub> monolayers (layer 1 and layer 3 in Fig. 5a) exhibit the same temperature dependence with a  $T_c$  of  $\sim 48$  K.

To further highlight the role of stacking engineering in affecting the local magnetic order and transition temperatures of small-twist-angle tDT CrI<sub>3</sub>, Fig. 5d plots a mean-field phase diagram of the normalized out-of-plane magnetization of CrI<sub>3</sub> layer 4 ( $m_{z4}$ ) as a function of temperature  $T$  and  $J_{\text{twist}}/J_M$  using our model. Here,  $J_{\text{twist}}$  is a variable interlayer exchange interaction at the twisted interface of tDT CrI<sub>3</sub>, and the sign of  $m_{z4}$  is defined in relative to the direction of the out-of-plane magnetization  $m_{z3}$  of the CrI<sub>3</sub> layer 3. When  $J_{\text{twist}}/J_M > 0$ , the system orders antiferromagnetically layer-wise below the  $T_c$  and  $m_{z4}$  is oppositely aligned with  $m_{z3}$  as shown in Fig. 5a. When  $J_{\text{twist}}/J_M < 0$ , the two twist-interfaced CrI<sub>3</sub> monolayers are ferromagnetically coupled and uncompensated net magnetic moment is formed in tDT CrI<sub>3</sub> below the magnetic critical temperature. Notably, as the magnitude of the FM-like coupling  $J_{\text{twist}}$  increases, the calculated  $T_c$  enhances from 48 K to 58 K when  $J_{\text{twist}}/J_M$  reaches  $-11.5$ , corresponding to the rhombohedral stacking case ( $J_{\text{twist}} = J_R$ ). In the high temperature regime, small-twist-angle tDT CrI<sub>3</sub> enters the paramagnetic phase where the long-range FM (AFM) order vanishes.

In summary, we have utilized scanning NV magnetometry techniques to investigate spatial and thermodynamic phase separation of moiré magnetism hosted by twisted CrI<sub>3</sub>. By using NV spin relaxometry methods to probe local spin fluctuations, we explicitly show that the co-existing FM-AFM phases within individual moiré supercells manifest distinct second-order magnetic phase transition points. The measured Curie temperature of rhombohedral (AB) stacking driven FM state is significantly higher than the Néel temperature of monoclinic (AB') stacking driven AFM one due to the spatially modulated exchange interaction at the twisted interface. In addition, we have directly visualized the stray field and magnetization maps across the magnetic phase transition points showing that twist engineering can effectively control the Curie temperature of local FM order in tDT CrI<sub>3</sub>. Our results are well rationalized by a proposed mean-field theoretical model, which captures the layer-resolved  $T_c$  in small-twist-angle tDT CrI<sub>3</sub>. When extending to other combinations of atomically thin twisted odd number of CrI<sub>3</sub> layers, we expect that the observed stacking order dependent magnetic phase transition with separate critical temperatures remains observable by the scanning NV quantum microscopy techniques. The presented results further highlight the opportunities provided by quantum spin sensors for investigating the local spin related phenomena in moiré quantum magnets. The stacking and temperature driven “intracell”

magnetic phase separations observed in twisted 2D magnets may also find relevant applications in realizing local control of functional material properties through carefully engineered proximity effect, advancing the current state of the art of vdW spintronic devices<sup>24,42</sup>.

**Data availability.** All data supporting the findings of this study are available from the corresponding author on reasonable request.

**Acknowledgements.** The authors are grateful to Rainer Stöhr and Sreehari Jayaram for valuable discussions on cryogenic NV measurement techniques. This work was primarily supported by U.S. Department of Energy (DOE), Office of Science, Basic Energy Sciences (BES), under award No. DE-SC0022946. Development of the cryogenic scanning NV microscopy was supported by the Air Force Office of Scientific Research (AFOSR) under grant No. FA9550-20-1-0319 and its Young Investigator Program under grant No. FA9550-21-1-0125. C. R. D. also acknowledges the support from the Office of Naval Research (ONR) under grant No. N00014-23-1-2146. L. Z. acknowledges the support from the U.S. Department of Energy (DOE), Office of Science, Basic Energy Science (BES), under award No. DE-SC0024145 (for the moiré magnets sample fabrication) and AFOSR YIP grant No. FA9550-21-1-0065 and Alfred. P. Sloan Foundation (for the instrument development of 2D vdW structure fabrication platform). A. S. and H. C. acknowledge the support from the National Science Foundation CAREER Grant No. DMR-1945023. R. H. acknowledges support from the Department of Energy, Basic Energy Sciences (DE-SC0024147). H. C. L. was supported by National Key R&D Program of China (Grant No. 2018YFE0202600 and 2022YFA1403800), the Beijing Natural Science Foundation (Grant No. Z200005), the National Natural Science Foundation of China (Grants No. 12174443), and the Beijing National Laboratory for Condensed Matter Physics.

**Author contributions.** S. L. performed the NV measurements and analyzed the data with N. M., M. H., H. L., and H. W. Z. S. and L. Z. prepared the CrI<sub>3</sub> devices. A. S. and H. C. performed the mean-field theoretical calculations. N. A., S. H. S., and R. H. performed the transmission electron microscopy characterizations. S. Y. and H. C. L. provided bulk CrI<sub>3</sub> crystals. C. R. D. supervised this project.

### **Competing interests**

The authors declare no competing interests.

## References

1. Xu, Y. *et al.* Coexisting ferromagnetic–antiferromagnetic state in twisted bilayer CrI<sub>3</sub>. *Nat. Nanotechnol.* **17**, 143–147 (2022).
2. Song, T. *et al.* Direct visualization of magnetic domains and moiré magnetism in twisted 2D magnets. *Science* **374**, 1140–1144 (2021).
3. Xie, H. *et al.* Twist engineering of the two-dimensional magnetism in double bilayer chromium triiodide homostructures. *Nat. Phys.* **18**, 30–36 (2022).
4. Cheng, G. *et al.* Electrically tunable moiré magnetism in twisted double bilayers of chromium triiodide. *Nat. Electron.* **6**, 434–442 (2023).
5. Xie, H. *et al.* Evidence of non-collinear spin texture in magnetic moiré superlattices *Nat. Phys.* **19**, 1150–1155 (2023).
6. Tong, Q., Liu, F., Xiao, J. & Yao, W. Skyrmions in the Moiré of van der Waals 2D magnets. *Nano. Lett.* **18**, 7194–7199 (2018).
7. Akram, M. *et al.* Moiré skyrmions and chiral magnetic phases in twisted CrX<sub>3</sub> (X = I, Br, and Cl) bilayers. *Nano. Lett.* **21**, 6633–6639 (2021).
8. Sivadas, N., Okamoto, S., Xu, X., Fennie, Craig. J. & Xiao, D. Stacking-dependent magnetism in bilayer CrI<sub>3</sub>. *Nano. Lett.* **18**, 7658–7664 (2018).
9. Wang, C., Gao, Y., Lv, H., Xu, X. & Xiao, D. Stacking domain wall magnons in twisted van der Waals magnets. *Phys. Rev. Lett.* **125**, 247201 (2020).
10. Hejazi, K., Luo, Z.-X. & Balents, L. Noncollinear phases in moiré magnets. *Proc. Natl. Acad. Sci.* **117**, 10721–10726 (2020).
11. Huang, M. *et al.* Revealing intrinsic domains and fluctuations of moiré magnetism by a wide-field quantum microscope. *Nat. Commun.* **14**, 5259 (2023).
12. Cao, Y. *et al.* Unconventional superconductivity in magic-angle graphene superlattices. *Nature* **556**, 43–50 (2018).
13. Balents, L., Dean, C. R., Efetov, D. K. & Young, A. F. Superconductivity and strong correlations in moiré flat bands. *Nat. Phys.* **16**, 725–733 (2020).
14. Andrei, E. Y. *et al.* The marvels of moiré materials. *Nat. Rev. Mater.* **6**, 201–206 (2021).
15. Kennes, D. M. *et al.* Moiré heterostructures as a condensed-matter quantum simulator. *Nat. Phys.* **17**, 155–163 (2021).
16. Wu, F., Lovorn, T., Tutuc, E. & MacDonald, A. H. Hubbard model physics in transition metal dichalcogenide moiré bands. *Phys. Rev. Lett.* **121**, 026402 (2018).
17. Huang, B. *et al.* Layer-dependent ferromagnetism in a van der Waals crystal down to the monolayer limit. *Nature* **546**, 270–273 (2017).
18. Thiel, L. *et al.* Probing magnetism in 2D materials at the nanoscale with single-spin microscopy. *Science* **364**, 973–976 (2019).
19. Niu, B. *et al.* Coexistence of magnetic orders in two-dimensional magnet CrI<sub>3</sub>. *Nano. Lett.* **20**, 553–558 (2020).
20. Degen, C. L., Reinhard, F. & Cappellaro, P. Quantum sensing. *Rev. Mod. Phys.* **89**, 035002 (2017).
21. Rondin, L. *et al.* Magnetometry with nitrogen-vacancy defects in diamond. *Rep. Prog. Phys.* **77**, 056503 (2014).
22. Doherty, M. W. *et al.* The nitrogen-vacancy colour centre in diamond. *Phys. Rep.* **528**, 1–45 (2013).
23. Geim, A. K. & Grigorieva, I. V. Van der Waals heterostructures. *Nature* **499**, 419–425 (2013).

24. Burch, K. S., Mandrus, D. & Park, J.-G. Magnetism in two-dimensional van der Waals materials. *Nature* **563**, 47–52 (2018).
25. Kim, K. *et al.* van der Waals heterostructures with high accuracy rotational alignment. *Nano. Lett.* **16**, 1989–1995 (2016).
26. Sung, S. H. *et al.* Torsional periodic lattice distortions and diffraction of twisted 2D materials. *Nat. Commun.* **13**, 7826 (2022).
27. Finco, A. *et al.* Imaging non-collinear antiferromagnetic textures via single spin relaxometry. *Nat. Commun.* **12**, 767 (2021).
28. Ku, M. J. H. *et al.* Imaging viscous flow of the Dirac fluid in graphene. *Nature* **583**, 537–541 (2020).
29. Pelliccione, M. *et al.* Scanned probe imaging of nanoscale magnetism at cryogenic temperatures with a single-spin quantum sensor. *Nat. Nanotechnol.* **11**, 700–705 (2016).
30. Casola, F., van der Sar, T. & Yacoby, A. Probing condensed matter physics with magnetometry based on nitrogen-vacancy centres in diamond. *Nat. Rev. Mater.* **3**, 17088 (2018).
31. McCullian, B. A. *et al.* Broadband multi-magnon relaxometry using a quantum spin sensor for high frequency ferromagnetic dynamics sensing. *Nat. Commun.* **11**, 5229 (2020).
32. Andersen, T. I. *et al.* Electron-phonon instability in graphene revealed by global and local noise probes. *Science* **364**, 154–157 (2019).
33. Flebus, B. & Tserkovnyak, Y. Quantum-impurity relaxometry of magnetization dynamics. *Phys. Rev. Lett.* **121**, 187204 (2018).
34. McLaughlin, N. J. *et al.* Quantum imaging of magnetic phase transitions and spin fluctuations in intrinsic magnetic topological nanoflakes. *Nano. Lett.* **22**, 5810–5817 (2022).
35. Ariyaratne, A., Bluvstein, D., Myers, B. A. & Jayich, A. C. B. Nanoscale electrical conductivity imaging using a nitrogen-vacancy center in diamond. *Nat. Commun.* **9**, 2406 (2018).
36. Du, C. *et al.* Control and local measurement of the spin chemical potential in a magnetic insulator. *Science* **357**, 195–198 (2017).
37. Yoo, H. *et al.* Atomic and electronic reconstruction at the van der Waals interface in twisted bilayer graphene. *Nat. Mater.* **18**, 448–453 (2019).
38. Jin, W. *et al.* Raman fingerprint of two terahertz spin wave branches in a two-dimensional honeycomb Ising ferromagnet. *Nat. Commun.* **9**, 5122 (2018).
39. Chen, L. *et al.* Topological spin excitations in honeycomb ferromagnet CrI<sub>3</sub>. *Phys. Rev. X* **8**, 041028 (2018).
40. Stanley, H. E. *Introduction to Phase Transitions and Critical Phenomena* (Oxford Univ Press, 1971).
41. Lee, T. D. & Yang, C. N. Statistical theory of equations of state and phase transitions. II. lattice gas and Ising model. *Phys. Rev.* **87**, 410–419 (1952).
42. Žutić, I., Fabian, J. & Das Sarma, S. Spintronics: fundamentals and applications. *Rev. Mod. Phys.* **76**, 323–410 (2004).

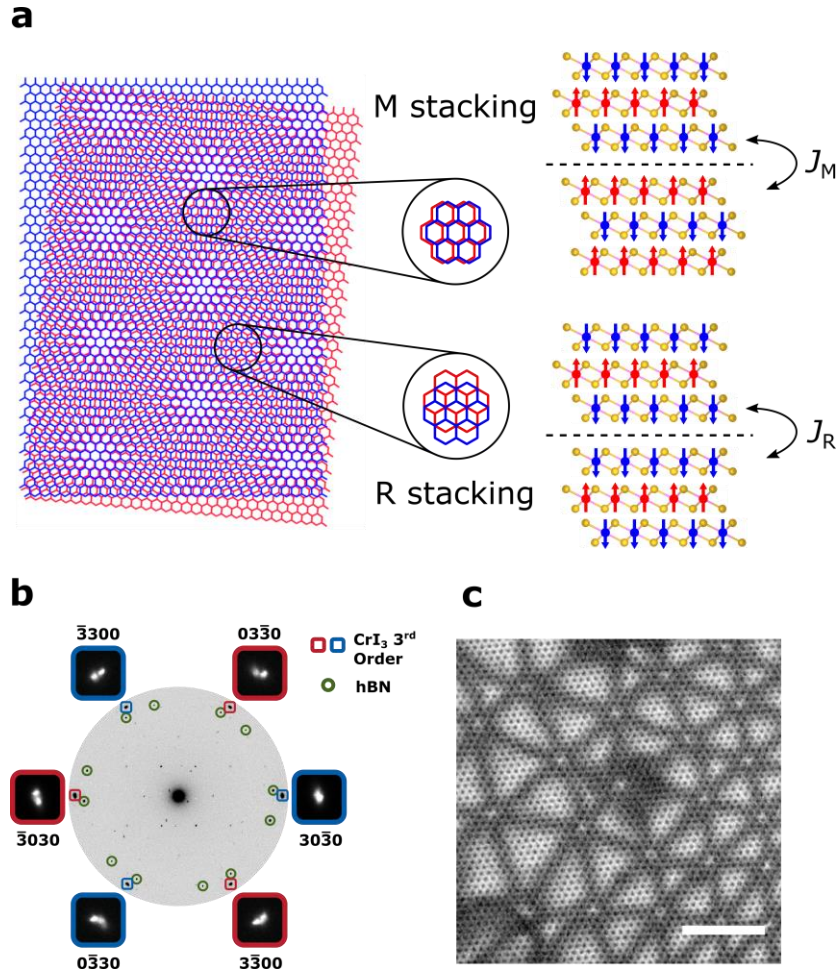


**Figure 1. Moiré superlattices of tDT CrI<sub>3</sub>.** **a** Left: Moiré superlattice structure of a small-twist-angle tDT CrI<sub>3</sub>. Only the two layers of Cr atoms adjacent to the twisted interface are shown for visual clarity. Cr atoms belonging to the top and bottom CrI<sub>3</sub> layers are labeled in blue and red colors, respectively. Right: Schematic of rhombohedral (AB) and monoclinic (AB') stacking driven FM and AFM orders in the magnetic ground state of small-twist-angle tDT CrI<sub>3</sub>. Magnetic moments carried by the middle two CrI<sub>3</sub> monolayers are ferromagnetically or antiferromagnetically coupled depending on the local interlayer exchange interaction  $J_R$  and  $J_M$  at the twisted interface. The blue and red arrows represent the local magnetic moment carried by Cr atoms (blue and red balls) at individual layers. The yellow balls represent the I atoms and the black dashed lines highlight the twisted interface. **b** SAED patterns of the fifth-order Bragg peaks of a  $\sim 0.8^\circ$  tDT CrI<sub>3</sub> device (blue and red rectangles) from a surveyed sample area of  $\sim 850$  nm  $\times$   $\sim 850$  nm. **c** BF-TEM real space image of a sample region showing the characteristic hexagonal superlattice structure in the  $\sim 0.8^\circ$  tDT CrI<sub>3</sub> device. The scale bar is 25 nm.

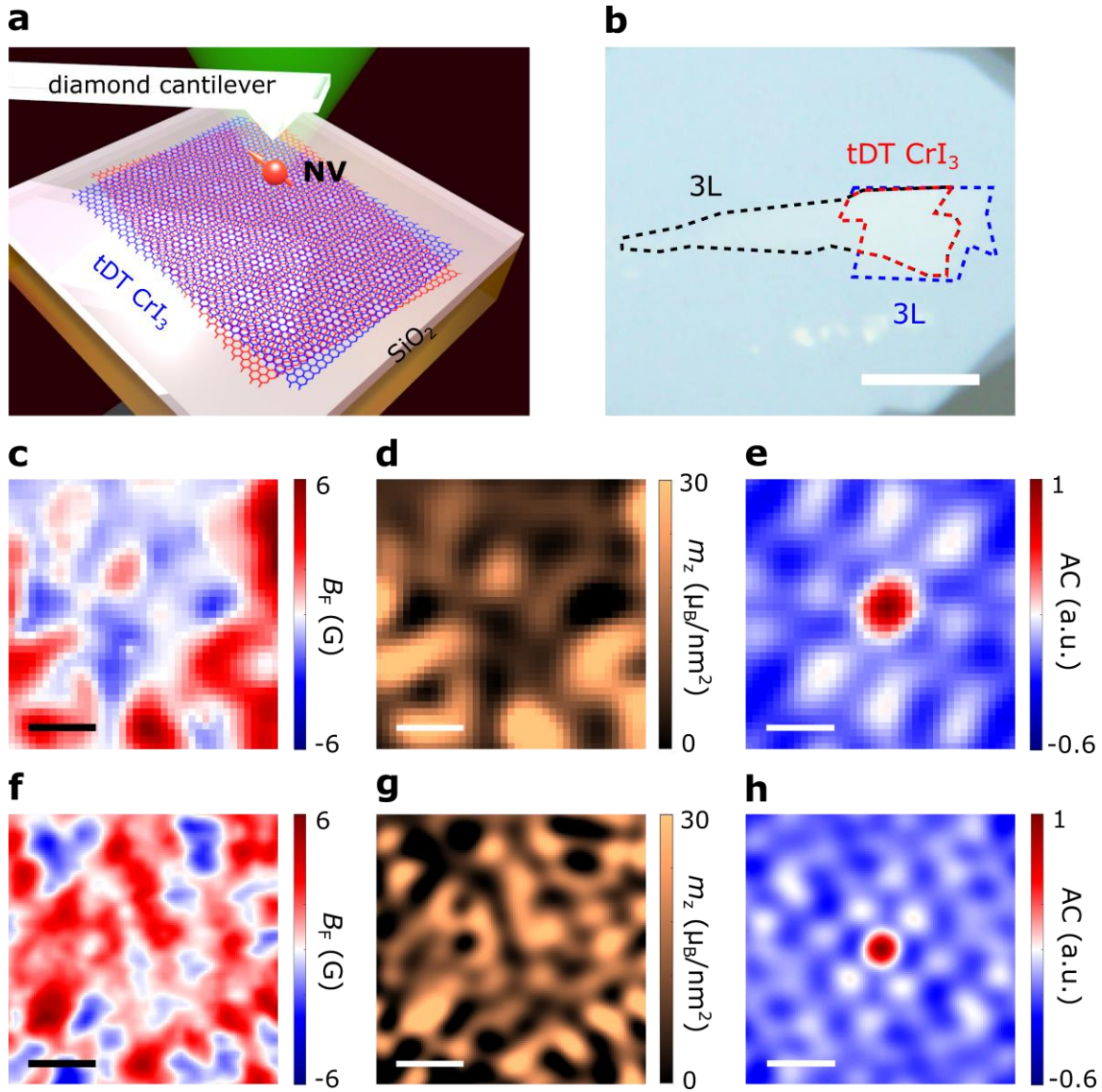


**Figure 2. Scanning single-spin magnetometry measurements of small-twist-angle tDT CrI<sub>3</sub>.** **a** Schematic illustration of scanning NV measurements of twisted CrI<sub>3</sub>. **b** Optical microscope image of a small-twist-angle tDT CrI<sub>3</sub> sample. The two torn trilayer CrI<sub>3</sub> flakes are outlined by the black and blue dashed lines, respectively, and the twisted area is highlighted by the red dashed lines. Scale bar is 10  $\mu\text{m}$ . **c, f** Nanoscale scanning NV imaging of magnetic stray fields emanating from selected sample areas of a 0.15° tDT CrI<sub>3</sub> (**c**) and a 0.25° tDT CrI<sub>3</sub> device (**f**). **d, g** Magnetization maps reconstructed from the stray field patterns shown in **c** and **f** for the 0.15° tDT CrI<sub>3</sub> (**d**) and 0.25° tDT CrI<sub>3</sub> (**g**) sample. **e, h** Normalized autocorrelation (AC) maps of the stray field patterns shown in **c** and **f** for the 0.15° tDT CrI<sub>3</sub> (**e**) and 0.25° tDT CrI<sub>3</sub> device (**h**). Scale bar is 200 nm for images presented from **c** to **h**.

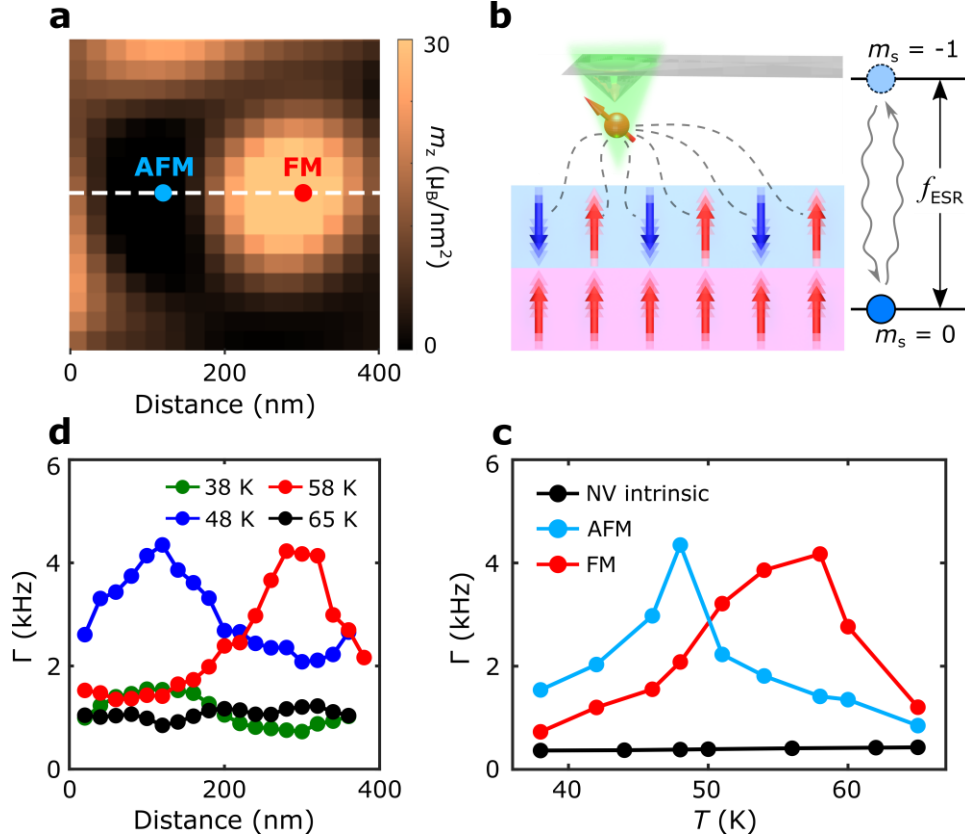


**Figure 3. NV spin relaxometry measurements of spin fluctuations in  $0.15^\circ$  tDT  $\text{CrI}_3$ .** **a** Zoomed-in view of a magnetization map measured on a selected sample area ( $400 \text{ nm} \times 400 \text{ nm}$ ) of the  $0.15^\circ$  tDT  $\text{CrI}_3$  device, showing co-existing FM and AFM domains. **b** Schematic of NV spin relaxometry measurements to probe spin fluctuations of local FM and AFM states in a proximal sample. The blue and red arrows represent local magnetic moments forming spontaneous AFM and FM orders. Noncoherent magnetic noise arising from FM or AFM spin fluctuations at the NV ESR frequencies  $f_{\text{ESR}}$  will drive NV spin transitions from the  $m_s = 0$  to the  $m_s = \pm 1$  state, resulting in enhanced NV relaxation rate. **c** Temperature dependence of NV spin relaxation rate  $\Gamma$  measured when the NV center is positioned right above the FM and AFM domains formed in the  $0.15^\circ$  tDT  $\text{CrI}_3$  sample. Control measurement results are also presented to characterize the intrinsic NV spin relaxation rate. **d** 1D NV spin relaxation rate  $\Gamma$  measured along the white dashed lines across the co-existing FM and AFM domains in the  $0.15^\circ$  tDT  $\text{CrI}_3$  device shown in Fig. 3a. The peak values of  $\Gamma$  measured at 48 K and 58 K occur at the corresponding in-plane lateral positions of AFM and FM domains, respectively.

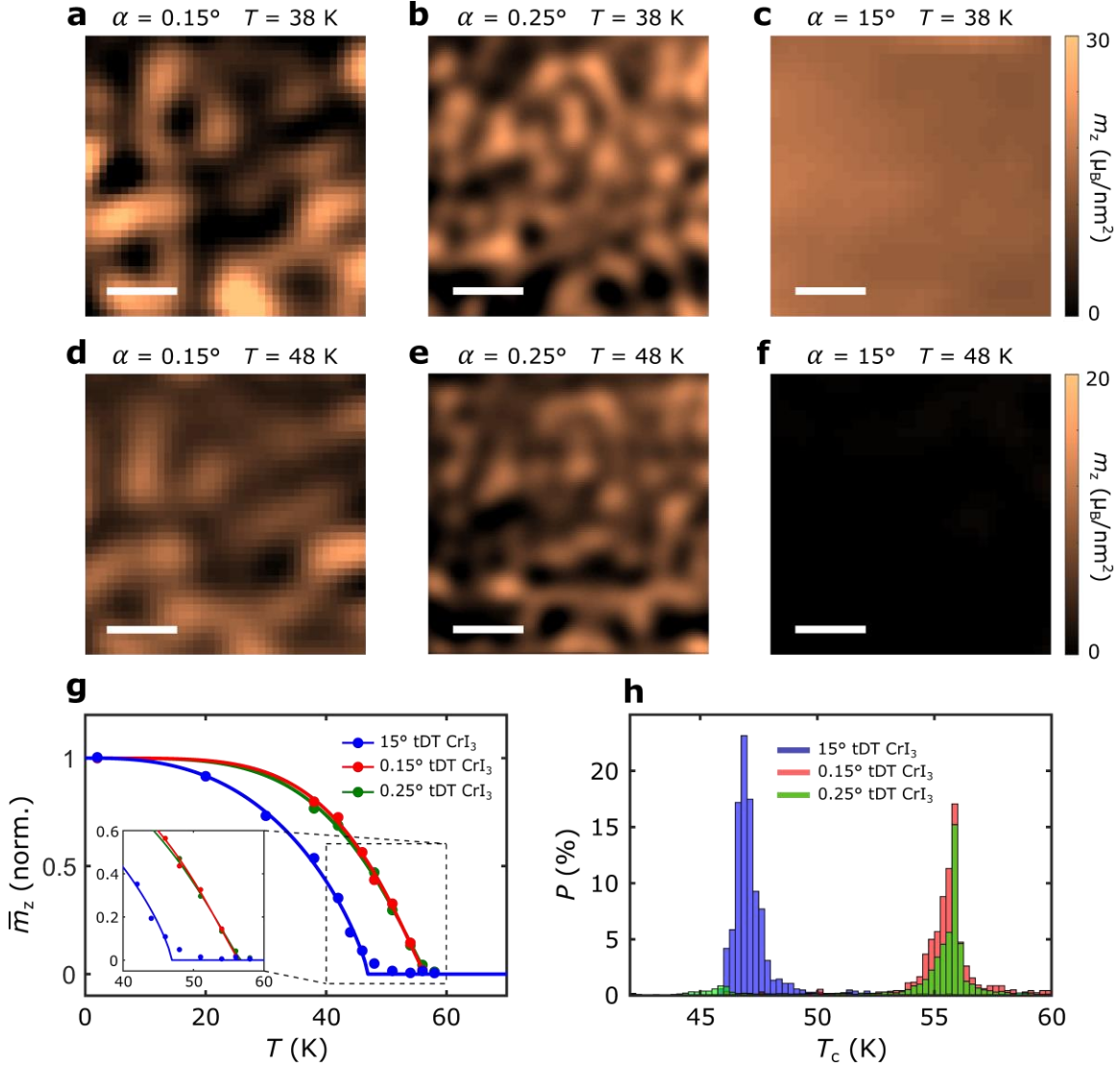


**Figure 4. Increased Curie temperatures of FM domains formed in small-twist-angle tDT  $\text{CrI}_3$ .** **a-c** Reconstructed magnetization maps of selected sample areas of  $0.15^\circ$  tDT  $\text{CrI}_3$  (**a**),  $0.25^\circ$  tDT  $\text{CrI}_3$  (**b**), and  $15^\circ$  tDT  $\text{CrI}_3$  (**c**) device measured at 38 K. **d-f** Reconstructed magnetization maps of the same sample areas of the  $0.15^\circ$  tDT  $\text{CrI}_3$  (**d**),  $0.25^\circ$  tDT  $\text{CrI}_3$  (**e**), and  $15^\circ$  tDT  $\text{CrI}_3$  (**f**) device measured at 48 K. Scale bar is 200 nm in Figs. 4a-4f. **g** Temperature dependence of average out-of-plane magnetization  $\bar{m}_z$  of FM domains formed in the selected sample areas of  $0.15^\circ$  tDT  $\text{CrI}_3$ ,  $0.25^\circ$  tDT  $\text{CrI}_3$ , and  $15^\circ$  tDT  $\text{CrI}_3$  device. Inset shows a zoomed-in view of the magnetic curves around transition temperatures. **h** Histograms of the obtained magnetic transition temperatures of individual FM domains formed in selected sample areas of  $0.15^\circ$  tDT  $\text{CrI}_3$ ,  $0.25^\circ$  tDT  $\text{CrI}_3$ , and  $15^\circ$  tDT  $\text{CrI}_3$  sample shown in Figs. 4a-4f.

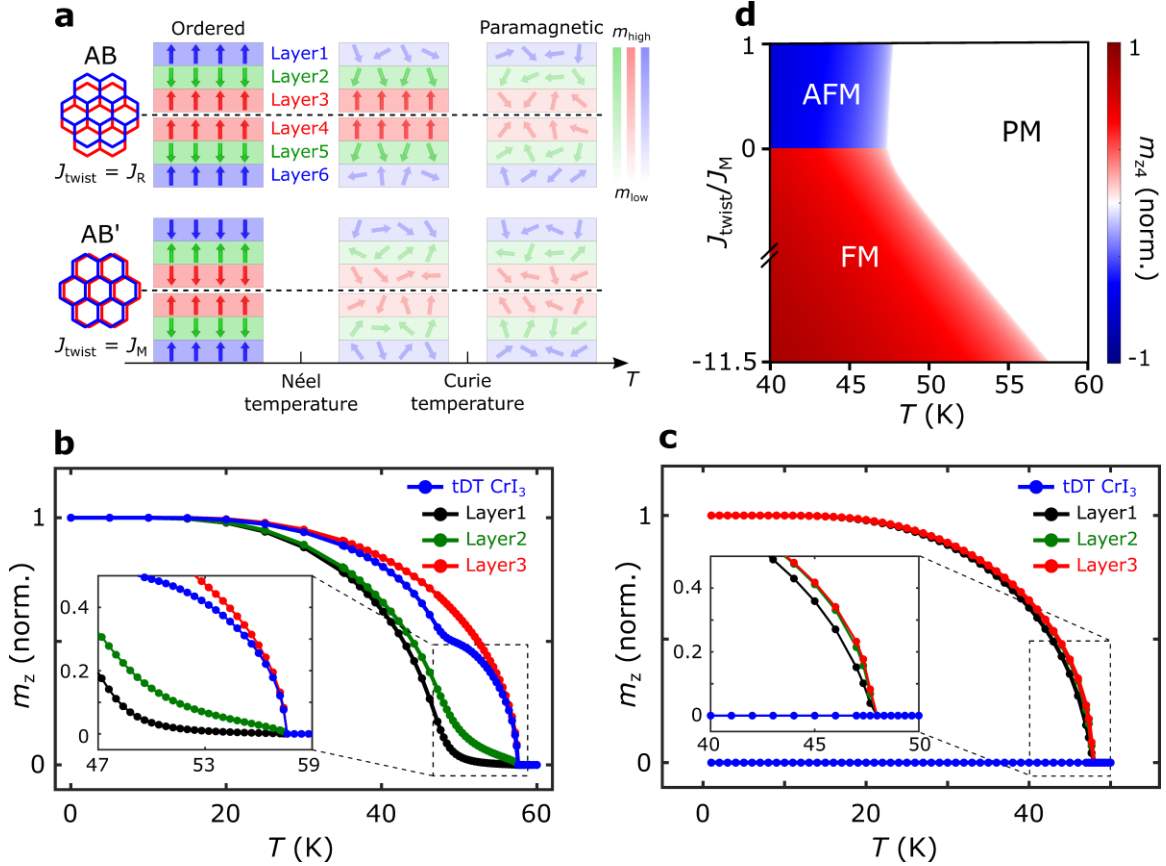


**Figure 5. Layer-resolved magnetic phases of small-twist-angle tDT CrI<sub>3</sub> with different stacking orders.** **a** Schematic of layer-resolved magnetic phases of rhombohedral (AB) and monoclinic (AB') stacked small-twist-angle tDT CrI<sub>3</sub> in ordered, intermediate, and paramagnetic state. The blue, red, and green arrows represent local magnetic moment carried by individual CrI<sub>3</sub> layers, and the fading background colors highlight the reduced magnetization with increasing temperature. Layers 1 to 6 are labelled from the top to bottom of tDT CrI<sub>3</sub> for reference. The black dashed lines highlight the twisted interface between the two CrI<sub>3</sub> trilayers. **b** Mean-field theory calculated temperature dependence of the normalized magnetization  $m_z$  of layer 1 (black), layer 2 (green), and layer 3 (red) of small-twist-angle tDT CrI<sub>3</sub> with rhombohedral (AB) stacking sequence. Normalized total net magnetization  $m_z$  curve of small-twist-angle tDT CrI<sub>3</sub> (blue) considering the overall contributions from the six CrI<sub>3</sub> layers is also presented. Inset shows a zoomed-in view of the features around the phase transition temperatures. **c** Calculated temperature dependent variations of the normalized magnetization  $m_z$  of layer 1 (black), layer 2 (green), and layer 3 (red) of small-twist-angle tDT CrI<sub>3</sub> with monoclinic (AB') stacking order. The total net magnetization curve of small-twist-angle tDT CrI<sub>3</sub> (blue) is also presented. Inset shows a zoomed-in view around the transition temperatures. **d** A constructed mean-field phase diagram of the normalized out-of-plane magnetization of CrI<sub>3</sub> layer 4 ( $m_{z4}$ ) as a function of temperature  $T$  and  $J_{\text{twist}}/J_M$ , highlighting the antiferromagnetic (AFM), ferromagnetic (FM), and paramagnetic (PM) states formed in small-twist-angle tDT CrI<sub>3</sub>.